

Thermoplastic moulding of regenerated silk

Chengchen Guo^{1,7}, Chunmei Li^{1,7*}, Hiep V. Vu², Philip Hanna³, Aron Lechtig³, Yimin Qiu¹, Xuan Mu¹, Shengjie Ling^{1,4}, Ara Nazarian^{3,5}, Samuel J. Lin⁶ and David L. Kaplan^{1*}

Early insights into the unique structure and properties of native silk suggested that β -sheet nanocrystallites in silk would degrade prior to melting when subjected to thermal processing. Since then, canonical approaches for fabricating silk-based materials typically involve solution-derived processing methods, which have inherent limitations with respect to silk protein solubility and stability in solution, and time and cost efficiency. Here we report a thermal processing method for the direct solid-state moulding of regenerated silk into bulk 'parts' or devices with tunable mechanical properties. At elevated temperature and pressure, regenerated amorphous silk nanomaterials with ultralow β -sheet content undergo thermal fusion via molecular rearrangement and self-assembly assisted by bound water to form a robust bulk material that retains biocompatibility, degradability and machinability. This technique reverses presumptions about the limitations of direct thermal processing of silk into a wide range of new material formats and composite materials with tailored properties and functionalities.

Silk is a natural protein-based biopolymer, which generally appears in fibre format and has outstanding mechanical properties; it is useful for fabricating durable textiles and has been used as clinical sutures for thousands of years^{1,2}. With the availability of modern characterization techniques, the unique properties of silks and the underlying mechanisms of protein self-assembly have been investigated^{3–10}. This improved fundamental understanding of silk, including protein composition, molecular structures and natural spinning mechanisms, has inspired new technologies to process silk by combining chemical, biological and engineering methodologies^{1,11–15}. Today, silk has been used as a material option in industries far beyond textiles, including use in biomaterials and scaffolds in biomedical applications, drug delivery, tissue engineering and regenerative medicine^{16–20}.

Natural silk is a semi-crystalline biopolymer material, consisting of β -sheet nanocrystallites embedded in a less-organized, less-crystalline continuous phase²¹. The strong hydrogen-bonding network in the β -sheet nanocrystallites contributes to the stability and robust mechanical properties of silks, which is the limitation in the thermal processing of silk to avoid degradation^{22–24}. Alternatively, considerable efforts have been made towards extracting and solubilizing silk protein (fibroin)^{25–28}, such as with concentrated LiBr solution to break the hydrogen-bond network within native spun fibres²⁵. This regenerated silk fibroin is then used in solution and reprocessed to generate new material formats including gels, films, sponges, fibres and related materials¹¹. However, these approaches require downstream processing, such as solvent removal or post-treatment with methanol or water vapour, to generate solution-stable silk-based materials. Solvent addition and removal, with the associated limits of solubility of the protein, lead to new and useful materials but at a significant cost because of various required processing steps both during and after material formation. The limitations in material properties are due to solubility constraints and the relatively short-term stability of silk in solution due to self-assembly²⁹.

Here, we report a new thermal processing method to transform solid-state regenerated natural silk directly into a robust structural

material with tunable mechanical properties, while retaining good machinability, biocompatibility and biodegradability. The new approach with fewer processing steps, lower cost, high protein density and broader functional material options mirrors more traditional thermal processing for synthetic polymers using pre-formed pellets and suggests new windows of opportunity for silk processing by overcoming the current limitations associated with solution-based processing approaches. This new method involves the fabrication of 'pellets', defined here as amorphous silk nanomaterials (ASN, with diameters from 30 nm to 1 μ m) reconstructed from regenerated aqueous silk fibroin solution. The pellets are treated by heat and pressure, leading to densification and fusion of the silk nanomaterials into bulk materials. The processed silk-based bulk materials are stronger than solution-derived materials, as well as superior when compared with most natural structural materials (for example, wood) and to some synthetic polymers. By tuning the processing conditions, the molecular structures and physical properties of the thermally processed silk-based bulk materials can be tailored to specific ranges while retaining the good machinability needed to form protein-based medical devices such as bone screws and ear tubes. Furthermore, a variety of functional molecules such as enzymes and antibiotics can be incorporated into the bulk materials as dopants to make silk-based functional composite devices.

Materials characterization

Combining top-down and bottom-up approaches to transform natural silk fibres into silk-based bulk parts via thermal processing first involves the production of ASN and then processing of ASN by hot pressing (Fig. 1a). This technique was used to directly mould silk bars, rods and plates, as well as to fabricate tubes and screws with machining (Fig. 1b–e). Natural silk fibres from silkworm (*Bombyx mori*) cocoons consist of sericin and silk fibroin, where silk fibroin is a native protein with a \sim 390 kDa heavy chain and a \sim 25 kDa light chain^{30,31}. By breaking the hydrogen-bond network in degummed (sericin-free) natural silk fibres (Fig. 2a–c) with concentrated salt solutions (such as LiBr), aqueous regenerated silk solutions are

¹Department of Biomedical Engineering, Tufts University, Medford, MA, USA. ²Department of Chemical and Biological Engineering, Tufts University, Medford, MA, USA. ³Center for Advanced Orthopedic Studies, Beth Israel Deaconess Medical Center, Harvard Medical School, Boston, MA, USA.

⁴School of Physical Science and Technology, ShanghaiTech University, Shanghai, China. ⁵Department of Orthopaedic Surgery, Yerevan State Medical University, Yerevan, Armenia. ⁶Divisions of Plastic Surgery and Otolaryngology, Beth Israel Deaconess Medical Center, Harvard Medical School, Boston, MA, USA. ⁷These authors contributed equally: Chengchen Guo, Chunmei Li. *e-mail: chunmei.li@tufts.edu; david.kaplan@tufts.edu

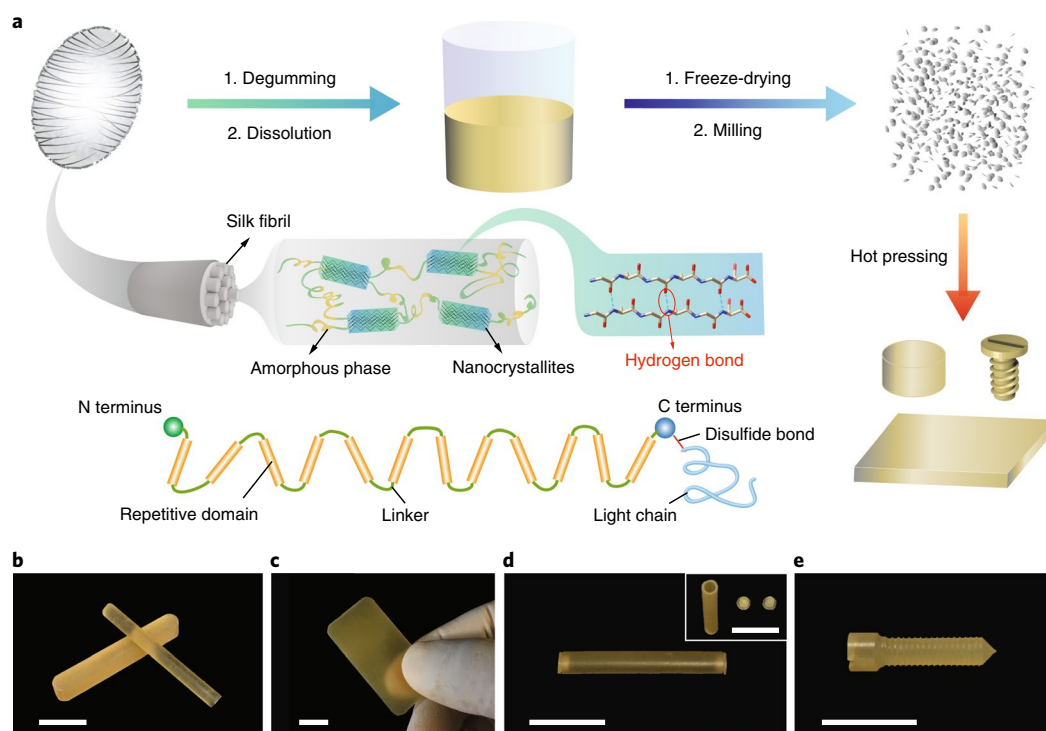


Fig. 1 | Process to generate silk-based bulk materials from native silk. **a**, Schematic combining top-down and bottom-up approaches to transform natural silk fibres into silk-based bulk materials by a thermal processing method. Step 1, chemical treatment to dissolve natural silk fibres and generate purified silk fibroin solution; step 2, freeze-drying and milling to generate amorphous silk nanomaterials; step 3, mechanical hot pressing with a high pressure for the densification, fusion and structural transition of the amorphous silk nanomaterials to semi-crystalline bulk materials. **b–e**, Photographs of silk objects, including a bar and rod (**b**), plate (**c**), tube with caps (**d**) and screw (**e**), fabricated by the thermal processing method with/without post-machining (scale bars are 1 cm).

obtained, in a similar format to the native liquid silk in the silkworm glands (Supplementary Fig. 1 and Supplementary Table 1)³². Fresh regenerated silk solution is then diluted, freeze-dried and milled to obtain ASN (Fig. 2d–f). Wide-angle X-ray scattering (WAXS), Fourier-transform infrared spectroscopy (FTIR) and solid-state NMR spectroscopy showed that the silk fibroin in ASN possessed significantly different molecular structures compared to those in natural silk fibres. The nanomaterials are primarily amorphous with a low content (<1.0%) of β -sheet structure and a high content of random coil or helical structures (Fig. 2g–j).

Structural tailoring of the silk fibroin at the molecular level supports options to tailor physical properties and inspires new routes for processing silk. Thermal analysis showed that the ASN had a water content of 5.0 ± 0.5 wt%, significantly higher than that found in degummed native silk fibres ($\sim 2.8 \pm 0.3$ wt%) (Supplementary Fig. 2a). Differential scanning calorimetry (DSC) showed that ASN had a defined water-associated glass transition temperature (T'_g) at 65 °C and a stable glass transition temperature at 178 °C (Supplementary Fig. 2b), which agrees well with previous studies on silk films prepared by solution casting and slow drying³³. A detailed stepwise scanning profile further indicated two types of bound water with ASN: weakly bound water with a maximum evaporation rate at 95 °C, and strongly bound water with a maximum evaporation rate at 125 °C (Supplementary Fig. 3). The bound water serves as a plasticizer, tuning the thermal properties of the silk materials. Previous studies with silk films have suggested that T'_g decreases as the residual water content increases^{34,35}. When heating the solution-casted silk films above T'_g , silk fibroin enters a viscoelastic liquid state prior to crystallization, which allows patterning, imprinting and film welding^{36,37}. By contrast, silk materials with a high content of β -sheet crystalline structure, such as native silk fibres, possess

challenges in thermal processing before degradation occurs due to the extreme stability of β -sheet crystalline structures^{22,23}. Recent investigations have shown that β -sheet crystalline structures can melt by fast laser heating upon input of heat energy alone, which suggests a useful way for thermally processing β -sheet-enriched biomaterials, but challenges remain on how to scale up to mould bulk materials³⁸.

Thermal processing of regenerated silk

Silk-based bulk materials were formed by direct thermal fusing the ASN at high pressure above T'_g . The ASN in powder form was first packed in a pre-designed aluminium mold, followed by hot pressing at high pressure (632 MPa in this study), and densified into bulk silk plates (Fig. 3a). Increasing the temperature of hot pressing densified the silk plates with a visual transition from white to transparent to pale yellow, indicating thermally driven structural changes at the microscale. Cross-sectional scanning electron microscopy (SEM) images showed that the ASN were loosely compacted at a lower processing temperature (25 °C) (Fig. 3a, A3) and tightly compacted at elevated processing temperatures (65 °C and 95 °C) with partial fusion (Fig. 3a, B3 and C3). When the processing temperature reached 125 °C, the ASN were more completely fused via collapsing to smaller globules with an average size of $\sim 30 \pm 5$ nm (Fig. 3a, D3, Supplementary Fig. 4), resulting in a similar size to the globules found in the silk solution self-assembly model^{39,40}. At still higher processing temperatures (145 °C, 175 °C), the nanosized silk globules further fused and underwent structural transitions to form more homogenous and fine interfaces (Fig. 3a, E3 and F3). NMR characterization of redissolved thermally processed bulk materials indicates that no severe degradation occurring to the silk fibroin was detected for all processing temperatures (Supplementary Fig. 5).

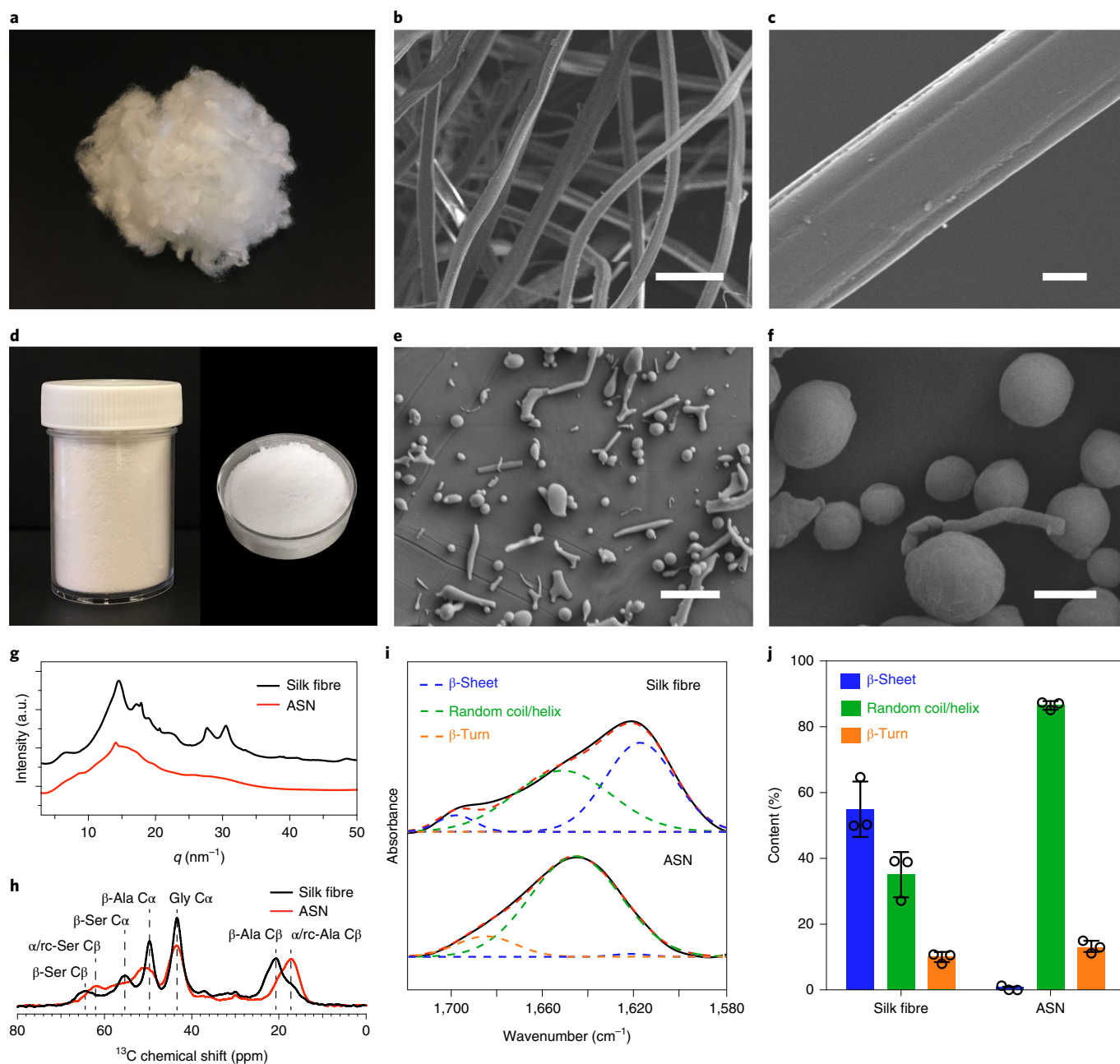


Fig. 2 | Comparison of degummed natural silk fibre and ASN. **a–c**, Photograph (**a**) and SEM images (**b,c**) of degummed natural silk fibres. **d–f**, Photograph (**d**) and SEM images (**e,f**) of ASN. **g**, One-dimensional WAXS profiles of degummed natural silk fibre and ASN. **h**, Solid-state ^{13}C NMR spectra of degummed natural silk fibre and ASN. **i**, FTIR spectra of degummed natural silk fibre and ASN. **j**, Quantitative analysis of secondary structures present in degummed silk fibre and ASN. Data are shown as mean \pm s.d.; $n=3$ independent experiments; the error bars represent the sample variation, measurement uncertainty and deconvolution uncertainty. Scale bars are 50 μm , 5 μm , 5 μm and 500 nm for **b**, **c**, **e** and **f**, respectively.

A combination of WAXS and FTIR characterizations identified significant β -sheet structure ($>40\%$) with increased crystallinity in silk plates processed at the higher temperatures (145 $^{\circ}\text{C}$, 175 $^{\circ}\text{C}$), while less of the β -sheet structure (~ 5 –15%) formed when processed at lower temperatures (25 $^{\circ}\text{C}$, 65 $^{\circ}\text{C}$ and 95 $^{\circ}\text{C}$) (Fig. 3b–e, Supplementary Fig. 6). In addition, WAXS revealed silk II structure (as in native silk fibres) when hot pressing was performed over 125 $^{\circ}\text{C}$, indicating a structural transition of silk fibroin to silk II structure (scattering vector $q = 14.6 \text{ nm}^{-1}$, d -spacing value of 4.3 \AA) during the processing (Fig. 3c)^{10,23}. In combination with thermal analysis of the ASN, structural characterizations of the processed bulk silk materials provide insight into the mechanism of thermal

fusing. At the cold state (25 $^{\circ}\text{C}$), a low content of β -sheet structure ($\sim 6.0 \pm 1.2\%$) was introduced by applying high pressure (shear) during the densification process (Supplementary Fig. 7). The density of the bulk material was $1.24 \pm 0.02 \text{ g cm}^{-3}$, lower than the density of the natural silk fibre ($\sim 1.35 \text{ g cm}^{-3}$; Supplementary Fig. 8). Increasing the processing temperature up to T'_g ($\sim 65 \text{ }^{\circ}\text{C}$) makes the density increase to $1.35 \pm 0.01 \text{ g cm}^{-3}$, indicating more densification due to the enhanced molecular mobility of silk fibroin chains. However, no significant β -sheet structure formation and crystallization occurred at this temperature. Increasing the processing temperature over T'_g further enhanced the molecular mobility of silk chains along with water removal, facilitating thermal fusion

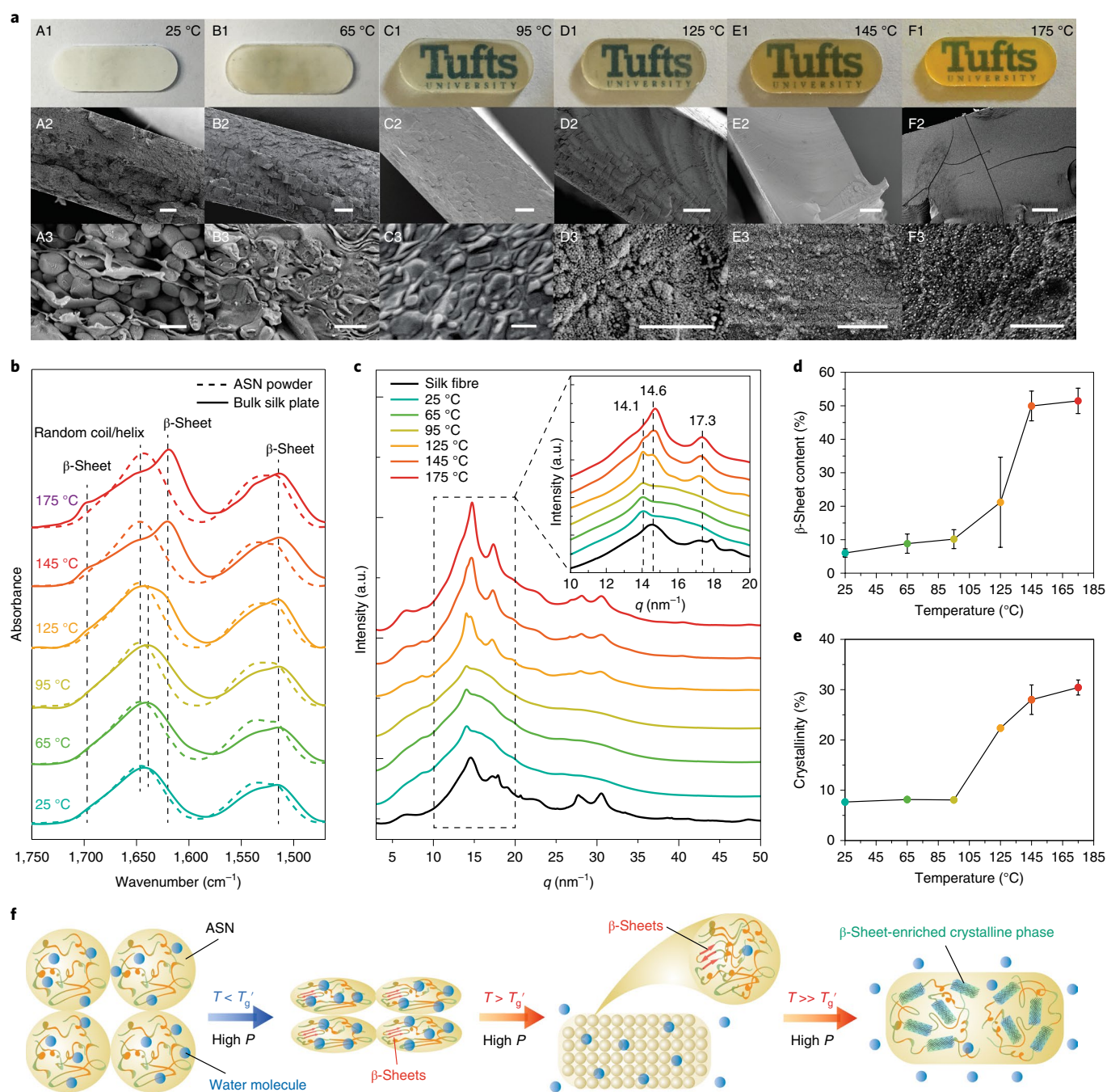


Fig. 3 | Thermal processing of ASN. **a**, Photographs and cross-sectional SEM images of the silk plates prepared at different temperatures: 25 °C (A1–A3), 65 °C (B1–B3), 95 °C (C1–C3), 125 °C (D1–D3), 145 °C (E1–E3) and 175 °C (F1–F3). **b**, FTIR spectra of ASN powder incubated at different temperatures for 15 min (dashed line) and bulk silk plates prepared at 632 MPa and different temperatures for 15 min (solid line). **c**, One-dimensional WAXS profiles of the bulk silk plates prepared at 632 MPa and different temperatures. Inset shows a zoomed-in plot for q values from 10 nm⁻¹ to 20 nm⁻¹. **d**, The β-sheet content of the silk plates quantified from FTIR spectra. Data are shown as mean ± s.d.; $n=3$ independent experiments. **e**, Degree of crystallinity of bulk silk plates estimated from 1D WAXS profiles. Data are shown as mean ± s.d.; $n=3$ independent experiments. **f**, Schematic showing a proposed mechanism for the structural transition of ASN during thermal processing. The scale bars in A2 to F2 and in A3 to F3 are 200 μm and 1 μm, respectively.

of silk fibroin (Fig. 3f). At 125 °C, a homogeneous fused state was achieved where silk forms nano-globules via molecular rearrangement and self-assembly^{39,40}. Further elevating the processing temperature over 125 °C allows removal of strongly bound water and sufficient molecular mobility of silk fibroin chains to overcome the energy barrier of structural transition, forming inter- and intra-molecular β-sheet nanocrystalline structures (Fig. 3f)^{35,39}. The presence of bound water in ASN is critical for structural transition

during thermal processing. Removal of bound water from ASN by preheating results in the failure of thermal moulding, which can, however, be reversed by moisture treatment to regain bound water (Supplementary Fig. 9). The thermal processing of ASN above T_g' also allows opportunities to fabricate sophisticated silk-based devices such as screws and contact lenses directly from ASN (Supplementary Fig. 10). The accompanying structural transition to β-sheet structures at high temperatures further offers options

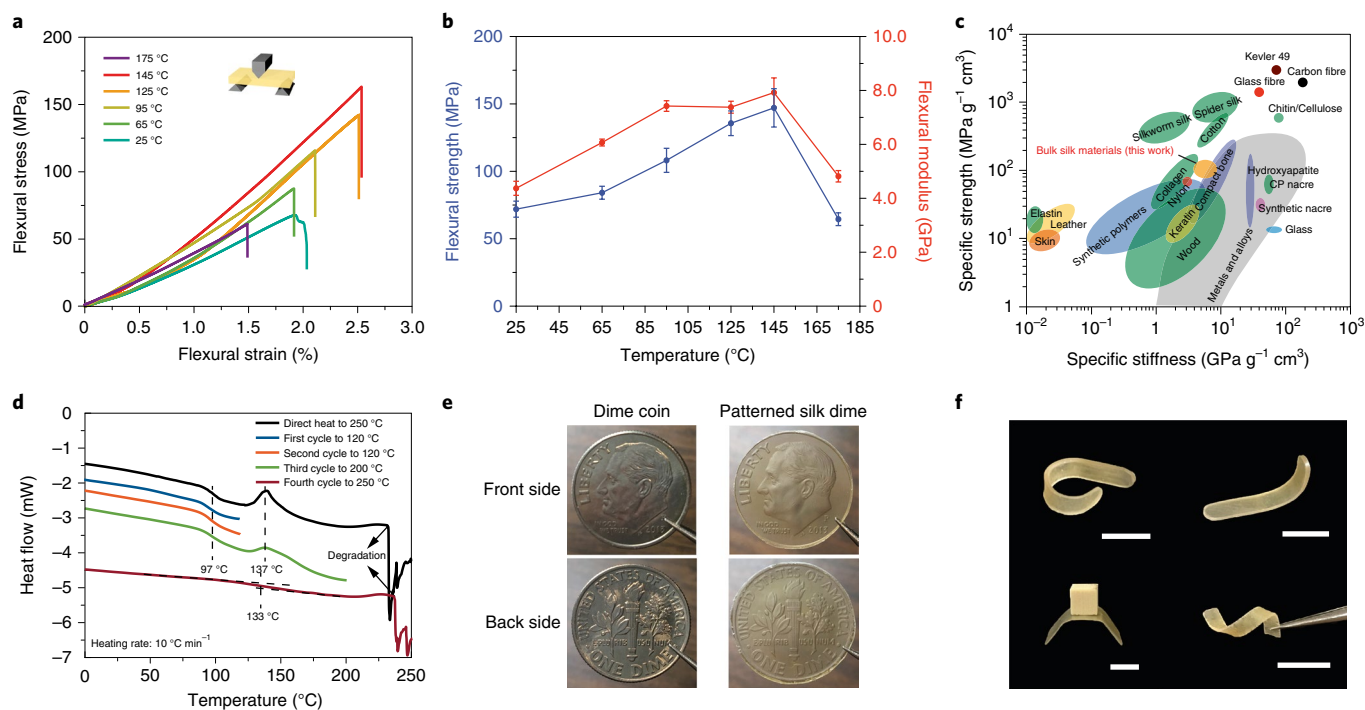


Fig. 4 | Physical properties of fabricated silk-based bulk materials. **a**, Three-point bending curves for silk plates prepared at different temperatures. **b**, Flexural strength and modulus of the silk plates prepared at different temperatures. Data are shown as mean \pm s.d.; $n = 3$ independent experiments. **c**, Comparison of the mechanical properties of the bulk silk materials with other natural and synthetic structural materials^{48,49}. CP, *Cristaria plicata*. **d**, DSC curves of the silk plates prepared at 125 °C and 632 MPa. **e–f**, Photographs of patterned silk dime (**e**) and silk structures (**f**) prepared by thermal forming. Scale bars in **f** are 1 cm.

to tune the physical properties and avoid complex post-processing treatments for silk-based devices.

Physical properties of silk-based bulk materials

The mechanical properties of the fabricated silk-based bulk materials were characterized with three-point bending, tensile and compression tests. The three-point bending test showed that the strength of the bulk silk materials increased with increasing processing temperature up to 145 °C (Fig. 4a,b). However, the strength decreased when processing at 175 °C, which is probably due to the slight thermal degradation of silk fibroin that is not detectable in NMR spectroscopy. Maximum strength was achieved for silk plates processed at 145 °C with a specific strength of 109 ± 10 MPa g⁻¹ cm³, which exceeds that of some natural structural materials such as *Cristaria plicata* nacre and wood (Fig. 4c). A similar trend was observed for the tensile and compression tests (Supplementary Fig. 11). Furthermore, lowering the processing pressure weakened the materials (Supplementary Fig. 12). In comparison with solution-based methods of fabricating silk bulk materials, this new thermal processing method produced silk materials with the best performance in compression tests (Supplementary Fig. 13)^{29,41–43}. Besides the excellent mechanical properties, the fabricated silk-based bulk materials possessed good thermal forming properties and machinability, supporting patterning, thermal moulding and machining. Figure 4d shows a DSC profile of silk materials processed at 125 °C and 632 MPa, indicating the materials had a stable glass-transition temperature of 97 °C and a crystallization temperature of 137 °C. As a result, the material became soft when heated above this glass-transition temperature to allow micro/nano-imprinting (Fig. 4e, Supplementary Fig. 14) and thermal forming to create designed constructs (Fig. 4f). Additionally, the silk-based bulk materials could be machined into rods, tubes, pins and medical devices such as bone screws and ear tubes (Supplementary Fig. 15).

Tailoring properties and functions of silk-based devices

The properties of fabricated silk-based devices, including degradability and swelling properties, can be controlled via manipulating the processing conditions. To demonstrate this point, silk-based bone screws were fabricated by machining silk bars prepared with different processing conditions (95 °C and 632 MPa; 125 °C and 632 MPa; 145 °C and 632 MPa) to vary the internal molecular structure and crystallinity. The *in vitro* degradation profiles indicated that the degradability of the silk bone screws was tunable, where processing at 145 °C and 632 MPa resulted in the slowest degradation rate in two enzyme solutions (protease XIV and α -chymotrypsin; Fig. 5a–c, Supplementary Fig. 16). In addition, *in vitro* water uptake in PBS solutions at 37 °C showed that the silk bone screws machined from silk bars prepared at 95 °C and 125 °C had rapid water uptake within 15 min with a maximum of ~30 wt% (Supplementary Fig. 17). In comparison, silk bone screws machined from silk bars prepared at 145 °C showed slower water uptake with a maximum of ~20 wt% (Supplementary Fig. 17). These differences reflect the underlying control of the molecular structure and crystallinity in silk-based devices by manipulating processing conditions. The silk bone screws showed good biocompatibility as implant devices, where they supported the formation of new bone structure on the screw surfaces without inflammation when implanted in rat femurs (Fig. 5d–f). The lining of multinucleated, macrophage-like cells along the threads also suggests early resorption of silk at the periphery of the devices. Another appealing feature of the thermal processing is its compatibility with bioactive molecules such as enzymes and antibiotics (Supplementary Fig. 18). The enhanced thermal stability of these molecules in the solid state, along with the stabilizing effect of silk with biological molecules, makes it possible to integrate those molecules into the bulk material to tailor biofunctions^{44,45}. As shown in Fig. 5g, silk ear tubes doped with protease XIV (doping ratio is 1 wt%)

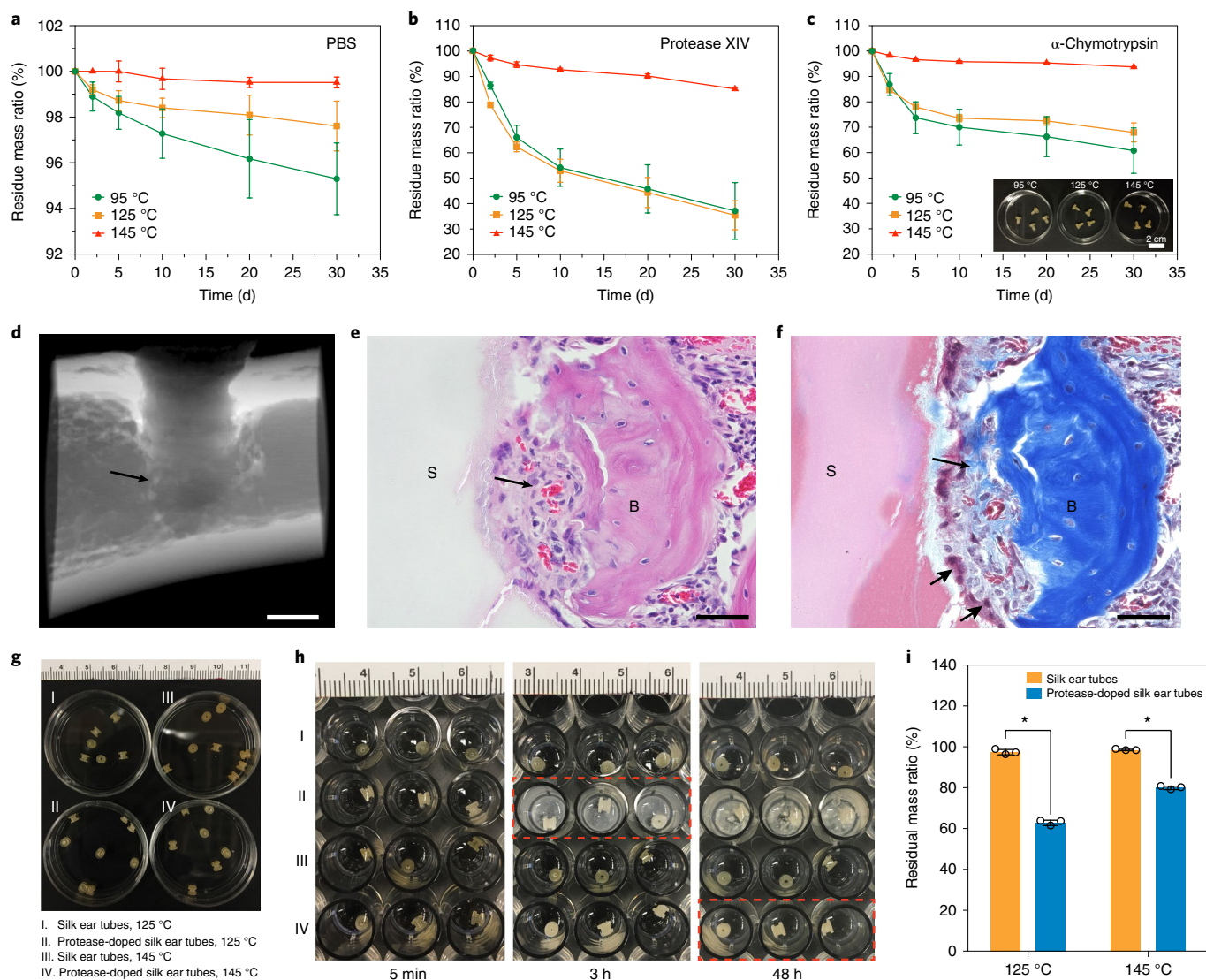


Fig. 5 | In vitro and in vivo testing of functional silk-based medical devices. **a–c**, In vitro degradation profiles of silk bone screws in PBS solution (**a**), protease XIV (5 U ml^{-1}) PBS solution (**b**) and α -chymotrypsin (40 U ml^{-1}) PBS solution (**c**). The silk bone screws were machined from bulk silk materials prepared at three different conditions (95°C , 632 MPa ; 125°C , 632 MPa ; 145°C , 632 MPa), and the photograph of as-fabricated silk screws is shown as an inset in **c**. Data are shown as mean \pm s.d.; $n = 3$ independent experiments. **d–f**, In vivo testing of silk bone screw (fabricated at 145°C , 632 MPa) after 4 weeks implantation in rats: images from micro-CT (**d**), hematoxylin and eosin staining (**e**) and Masson trichrome staining (**f**) demonstrated active new bone formation (long arrow) observed at the screw (S) surface along with multinucleated, macrophage-like cells (short arrow) lining the screw surface. B, adjacent bone. Data are shown as mean \pm s.d.; $n = 3$ independent experiments. Scale bars are 1 mm (**d**) and $50 \mu\text{m}$ (**e,f**). **g**, Photographs of fabricated silk ear tubes with or without protease XIV doping ($1 \text{ wt}\%$). The silk ear tubes were machined from pure silk or silk–protease XIV bulk materials prepared at two different conditions (125°C , 632 MPa ; 145°C , 632 MPa). **h–i**, In vitro degradation analysis of silk ear tubes with or without protease XIV doping: photographs of silk ear tubes incubated in PBS at 37°C for different times (5 min, 3 h and 48 h, **h**) and residual mass ratios of silk ear tubes after continuous incubation in PBS at 37°C for 72 h (**i**). Red dashed lines in **h** indicate the observed degradation of silk ear tubes. The asterisks in **i** denote statistically significant differences obtained from two-way analysis of variance (ANOVA) analysis, $P < 0.0001$.

were successfully fabricated with thermal processing to enhance the degradability of the devices, showing a great advantage over solution-based methods since protease XIV would degrade the silk fibroin in solution. Once incubated in PBS at 37°C , the silk ear tubes doped with protease XIV show faster degradation than pure silk ear tubes prepared at the same conditions (Fig. 5h). Furthermore, the doped silk ear tubes made at 145°C and 632 MPa show slower degradation than the doped silk ear tubes made at 125°C and 632 MPa , which demonstrates the tunability of the thermal processing (Fig. 5h, Supplementary Fig. 19). The doped silk ear tubes made at 125°C and 145°C show residual mass ratios

of $62.8 \pm 1.3\%$ and $79.9 \pm 0.8\%$, respectively, after 72 h continuous incubation in PBS solutions (Fig. 5i).

Outlook

At high pressure and elevated temperature, the free-energy change of materials (Gibbs free energy $G = U + PV - TS$) may allow opportunities to tune phases or molecular structures in materials, which inspired us to investigate how external factors (pressure or temperature) influence silk self-assembly in the solid state as a new silk-processing strategy. Native silk fibroin self-assembles to form semi-crystalline block copolymer structures, whereby aligned

β -sheet nanocrystallites provide rigidity, and an amorphous matrix promotes flexibility. Such nature-optimized stable structures challenge direct thermal processing of native silk fibroin (sericin free) with common techniques used in traditional polymer engineering⁴⁶. The work reported here demonstrated good thermoplastic properties of regenerated ASN, offering a time- and cost-effective way to directly process silk fibroin materials in the solid state for fabricating 3D bulk protein-based biomaterials (see the Supplementary Note for a cost, time and energy assessment of different techniques used to process silk into bulk materials). Compared with native semi-crystalline silk, regenerated ASN have a well-defined water-associated glass-transition temperature at a relatively low temperature, a benefit in thermal moulding. The reported thermal processing method not only provides good control over structural, mechanical and degradation properties for the products but also shows excellent compatibility with bioactive molecules. More importantly, regenerated ASN were stable and can be stored over a long time period⁴⁷, which circumvents the limitations of solution-based processing methods and ensures the reproducibility and scalability of this method.

Online content

Any methods, additional references, Nature Research reporting summaries, source data, extended data, supplementary information, acknowledgements, peer review information; details of author contributions and competing interests; and statements of data and code availability are available at <https://doi.org/10.1038/s41563-019-0560-8>.

Received: 30 December 2018; Accepted: 8 November 2019;
Published online: 16 December 2019

References

- Vepari, C. & Kaplan, D. L. Silk as a biomaterial. *Prog. Polym. Sci.* **32**, 991–1007 (2007).
- Vollrath, F. & Porter, D. Spider silk as archetypal protein elastomer. *Soft Matter* **2**, 377–385 (2006).
- Vollrath, F. & Knight, D. P. Liquid crystalline spinning of spider silk. *Nature* **410**, 541–548 (2001).
- Shao, Z. Z. & Vollrath, F. Materials: surprising strength of silkworm silk. *Nature* **418**, 741 (2002).
- Jin, H. J. & Kaplan, D. L. Mechanism of silk processing in insects and spiders. *Nature* **424**, 1057–1061 (2003).
- Askarieh, G. et al. Self-assembly of spider silk proteins is controlled by a pH-sensitive relay. *Nature* **465**, 236–238 (2010).
- Hagn, F. et al. A conserved spider silk domain acts as a molecular switch that controls fibre assembly. *Nature* **465**, 239–242 (2010).
- Andersson, M., Johansson, J. & Rising, A. Silk spinning in silkworms and spiders. *Int. J. Mol. Sci.* **17**, 1290–1303 (2016).
- Yarger, J. L., Cherry, B. R. & van der Vaart, A. Uncovering the structure-function relationship in spider silk. *Nat. Rev. Mater.* **3**, 18008–18018 (2018).
- Guo, C. et al. Structural comparison of various silkworm silks: an insight into the structure-property relationship. *Biomacromolecules* **19**, 906–917 (2018).
- Rockwood, D. N. et al. Materials fabrication from *Bombyx mori* silk fibroin. *Nat. Protoc.* **6**, 1612–1631 (2011).
- Teule, F. et al. A protocol for the production of recombinant spider silk-like proteins for artificial fiber spinning. *Nat. Protoc.* **4**, 341–355 (2009).
- Heim, M., Keerl, D. & Scheibel, T. Spider silk: from soluble protein to extraordinary fiber. *Angew. Chem. Int. Edit.* **48**, 3584–3596 (2009).
- Andersson, M. et al. Biomimetic spinning of artificial spider silk from a chimeric minispidroin. *Nat. Chem. Biol.* **13**, 262–264 (2017).
- Zhou, Z. et al. Engineering the future of silk materials through advanced manufacturing. *Adv. Mater.* **30**, 1706983–1707008 (2018).
- Kundu, B., Rajkhowa, R., Kundu, S. C. & Wang, X. Silk fibroin biomaterials for tissue regenerations. *Adv. Drug Deliv. Rev.* **65**, 457–470 (2013).
- Abbott, R. D., Kimmerling, E. P., Cairns, D. M. & Kaplan, D. L. Silk as a biomaterial to support long-term three-dimensional tissue cultures. *ACS Appl. Mater. Interfaces* **8**, 21861–21868 (2016).
- Bhattacharjee, P. et al. Silk scaffolds in bone tissue engineering: an overview. *Acta Biomater.* **63**, 1–17 (2017).
- Crivelli, B. et al. Silk nanoparticles: from inert supports to bioactive natural carriers for drug delivery. *Soft Matter* **14**, 546–557 (2018).
- Holland, C., Numata, K., Rnjak-Kovacina, J. & Seib, F. P. The biomedical use of silk: past, present, future. *Adv. Healthc. Mater.* **8**, 1800465–1800490 (2019).
- Koh, L.-D. et al. Structures, mechanical properties and applications of silk fibroin materials. *Prog. Polym. Sci.* **46**, 86–110 (2015).
- Pauling, L. & Corey, R. B. The pleated sheet, a new layer configuration of polypeptide chains. *Proc. Natl Acad. Sci. USA* **37**, 251–256 (1951).
- Marsh, R. E., Corey, R. B. & Pauling, L. An investigation of the structure of silk fibroin. *Biochim. Biophys. Acta* **16**, 1–34 (1955).
- Keten, S., Xu, Z., Ihle, B. & Buehler, M. J. Nanoconfinement controls stiffness, strength and mechanical toughness of beta-sheet crystals in silk. *Nat. Mater.* **9**, 359–367 (2010).
- Liang, C. X. & Hirabayashi, K. Influence of solvation temperature on the molecular-features and physical-properties of fibroin membrane. *Polymer* **33**, 4388–4393 (1992).
- Trabicc, K. A. & Yager, P. Comparative structural characterization of naturally- and synthetically-spun fibers of *Bombyx mori* fibroin. *Macromolecules* **31**, 462–471 (1998).
- Ha, S. W., Tonelli, A. E. & Hudson, S. M. Structural studies of *Bombyx mori* silk fibroin during regeneration from solutions and wet fiber spinning. *Biomacromolecules* **6**, 1722–1731 (2005).
- Cheng, G., Wang, X., Tao, S., Xia, J. & Xu, S. Differences in regenerated silk fibroin prepared with different solvent systems: from structures to conformational changes. *J. Appl. Polym. Sci.* **132**, 41959–41966 (2015).
- Marelli, B. et al. Programming function into mechanical forms by directed assembly of silk bulk materials. *Proc. Natl Acad. Sci. USA* **114**, 451–456 (2017).
- Yamaguchi, K. et al. Primary structure of the silk fibroin light chain determined by cDNA sequencing and peptide analysis. *J. Mol. Biol.* **210**, 127–139 (1989).
- Zhou, C. Z. et al. Silk fibroin: structural implications of a remarkable amino acid sequence. *Proteins* **44**, 119–122 (2001).
- Suzuki, Y., Yamazaki, T., Aoki, A., Shindo, H. & Asakura, T. NMR study of the structures of repeated sequences, GAGXGA (X = S, Y, V), in *Bombyx mori* liquid silk. *Biomacromolecules* **15**, 104–112 (2014).
- Hu, X., Kaplan, D. & Cebe, P. Effect of water on the thermal properties of silk fibroin. *Thermochim. Acta* **461**, 137–144 (2007).
- Agarwal, N., Hoagland, D. A. & Farris, R. J. Effect of moisture absorption on the thermal properties of *Bombyx mori* silk fibroin films. *J. Appl. Polym. Sci.* **63**, 401–410 (1997).
- Yazawa, K., Ishida, K., Masunaga, H., Hikima, T. & Numata, K. Influence of water content on the beta-sheet formation, thermal stability, water removal, and mechanical properties of silk materials. *Biomacromolecules* **17**, 1057–1066 (2016).
- Brenckle, M. A. et al. Protein-protein nanoimprinting of silk fibroin films. *Adv. Mater.* **25**, 2409–2414 (2013).
- Brenckle, M. A. et al. Methods and applications of multilayer silk fibroin laminates based on spatially controlled welding in protein films. *Adv. Funct. Mater.* **26**, 44–50 (2016).
- Cebe, P. et al. Beating the heat—fast scanning melts silk beta sheet crystals. *Sci. Rep.* **3**, 1130–1136 (2013).
- Lu, Q. et al. Silk self-assembly mechanisms and control from thermodynamics to kinetics. *Biomacromolecules* **13**, 826–832 (2012).
- Koebly, S. R. et al. Silk reconstitution disrupts fibroin self-assembly. *Biomacromolecules* **16**, 2796–2804 (2015).
- Perrone, G. S. et al. The use of silk-based devices for fracture fixation. *Nat. Commun.* **5**, 3385–3393 (2014).
- Li, C. et al. Regenerated silk materials for functionalized silk orthopedic devices by mimicking natural processing. *Biomaterials* **110**, 24–33 (2016).
- Liu, K. et al. A silk cranial fixation system for neurosurgery. *Adv. Healthc. Mater.* **7**, 1701359–1701371 (2018).
- Guziewicz, N. A., Massetti, A. J., Perez-Ramirez, B. J. & Kaplan, D. L. Mechanisms of monoclonal antibody stabilization and release from silk biomaterials. *Biomaterials* **34**, 7766–7775 (2013).
- Li, A. B., Kluge, J. A., Guziewicz, N. A., Omenetto, F. G. & Kaplan, D. L. Silk-based stabilization of biomacromolecules. *J. Control. Release* **219**, 416–430 (2015).
- Lee, J. H. et al. Preparation of new natural silk non-woven fabrics by using adhesion characteristics of sericin and their characterization. *Int. J. Biol. Macromol.* **106**, 39–47 (2018).
- Kluge, J. A., Kahn, B. T., Brown, J. E., Omenetto, F. G. & Kaplan, D. L. Optimizing molecular weight of lyophilized silk as a shelf-stable source material. *ACS Biomater. Sci. Eng.* **2**, 595–605 (2016).
- Wegst, U. G., Bai, H., Saiz, E., Tomsia, A. P. & Ritchie, R. O. Bioinspired structural materials. *Nat. Mater.* **14**, 23–36 (2015).
- Mao, L. B. et al. Synthetic nacre by predesigned matrix-directed mineralization. *Science* **354**, 107–110 (2016).

Publisher's note Springer Nature remains neutral with regard to jurisdictional claims in published maps and institutional affiliations.

© The Author(s), under exclusive licence to Springer Nature Limited 2019

Methods

Regenerated silk fibroin preparation. *Bombyx mori* cocoons were cut into small pieces and boiled in an aqueous 0.02 M Na₂CO₃ (Sigma-Aldrich) solution for 30 min, followed by rinsing in distilled water to remove the Na₂CO₃ and sericin. The degummed silk was allowed to dry at room temperature overnight. The dried silk was dissolved in 9.3 M LiBr (Sigma-Aldrich) solution at 60 °C for 3–4 h. The solution was subsequently dialysed for 3 d in distilled water using Slide-a-Lyzer dialysis cassettes (MWCO 3,500, Pierce). The water was changed five times during the dialysis (1 h, 4 h, 8 h, 24 h, 48 h). After dialysis, the solution was centrifuged for 20 min at 9,780g twice to remove insoluble impurities. The concentration of the final silk solution was determined by measuring a volume of solution and the final dried weight (~6 wt.v.%). The solution was diluted and frozen using liquid nitrogen. The frozen silk solution was then lyophilized at –80 °C and 0.006 bar until complete sublimation. The lyophilized silk was then milled into ultrafine powders using a high-speed analytical mill (20,000 r.p.m., 2 min, Col-Parmer), giving the product referred to as amorphous silk nanomaterials (ASN). The ASN were stored in ambient dry conditions to prevent any rehydration until used in the processing steps below.

Hot pressing of ASN. ASN were packed into pre-designed moulds, followed by hot pressing at 632 MPa and variable temperatures (25 °C, 65 °C, 95 °C, 125 °C, 145 °C, 175 °C) for 15 min. After hot pressing, the samples were cooled down to room temperature and used for the characterizations. To incorporate bioactive molecules in the system, the silk powder was doped with ciprofloxacin hydrochloride (5 wt%, Sigma-Aldrich), gentamicin sulfate (5 wt%, Sigma-Aldrich), horseradish peroxidase (1 wt%, Sigma-Aldrich) and protease XIV (1 wt%, Sigma-Aldrich) by thorough mixing and subjected to hot pressing.

NMR spectroscopy. For structural characterization of the fresh regenerated silk solution, solution NMR experiments were performed on a Bruker 850 MHz Avance IIIHD spectrometer equipped with a 5 mm cryogenically helium-cooled triple-resonance TCL CryoProbe. The Larmor frequencies of ¹H, ¹³C and ¹⁵N were 850.28 MHz, 213.82 MHz and 86.17 MHz, respectively. A sealed capillary containing D₂O was used for NMR locking. Nuclear Overhauser effect spectroscopy (NOESY) was performed with a mixing time of 150 ms, 11 ppm spectral width in both the *t*₁ and *t*₂ dimensions, 512 and 2,048 complex points in the *t*₁ and *t*₂ dimensions respectively, 16 scans and a relaxation delay of 1 s. Total correlation spectroscopy (TOCSY) was performed with a mixing time of 60 ms, 11 ppm spectral width in both the *t*₁ and *t*₂ dimensions, 512 and 2,048 complex points in the *t*₁ and *t*₂ dimensions respectively, 16 scans and a relaxation delay of 1 s. Heteronuclear single quantum coherence (HSQC) data for ¹H–¹³C were collected with 165.8 ppm spectral width in the *t*₁ and 11 ppm spectral width in the *t*₂ dimensions, 256 and 1,024 complex points in *t*₁ and *t*₂ dimensions respectively, and 64 scans. HSQC data for ¹H–¹⁵N were collected with 28.0 ppm spectral width in the *t*₁ and 11 ppm spectral width in the *t*₂ dimensions, 512 and 1,024 complex points in *t*₁ and *t*₂ dimensions respectively, and 32 scans. The solid-state NMR spectra were collected on a Varian VNMRs 400 MHz spectrometer equipped with a 3.2 mm triple-resonance probe operating in double-resonance (¹H/¹³C) mode. The cross-polarization (CP) condition for ¹H→¹³C cross-polarization magic angle spinning (CP-MAS) experiments consisted of a 2.25 μs ¹H π/2 pulse, followed by a 1.0 ms ramped (3%) ¹H spin-lock pulse of 70 kHz radio frequency field strength. The experiments were performed with a 25 kHz sweep width, a recycle delay of 3.0 s, 8,192 scans and a two-pulse phase-modulated ¹H decoupling level of 91 kHz at a magic angle spinning speed of 20 kHz for all samples. A single NMR spectrum was obtained for each sample.

For structural characterization of processed silk-based bulk materials, 30 mg of silk-based bulk material prepared at different conditions was first solubilized in 3 ml of 9.3 M LiBr solution at 60 °C overnight to achieve complete dissolution. Then the solution was dialysed using 3.5 kDa (molecular weight) cut-off Slide-A-Lyzer Cassettes (Thermo Fisher) against deionized water for 3 d with the water changed six times. After dialysis, the solution was centrifuged for 20 min at 9,780 *x*_g twice to remove insoluble impurities. The concentration of the silk solution obtained was ~0.35 wt%. Then 500 μl of silk solution was freeze-dried and redissolved in 600 μl D₂O for ¹H NMR characterizations. Solution ¹H NMR spectroscopy experiments were performed on a Bruker 500 MHz spectrometer. The ¹H NMR spectra were collected with a sweep width of 10,000 Hz, an acquisition time of 3.28 s, a recycle delay of 0.5 s and 128 scans. A single NMR spectrum was obtained for each sample.

Thermal analysis. The thermal degradation of the silk samples was measured by thermogravimetric analysis from 30 to 800 °C in N₂ (99.99%) with a scanning speed of 5 °C min⁻¹. For all measurements, samples were kept under N₂ in the furnace to reach a stable weight prior to heating. DSC measurements were carried out on a TA Instruments Q100 calorimeter under a dry N₂ gas flow of 50 ml min⁻¹ with samples encapsulated in aluminium pans. Both standard DSC and temperature-modulated DSC (TMDSC) measurements were performed. In standard DSC measurements, the samples were heated from –50 to 200 °C with a heating rate of 10 °C min⁻¹. In TMDSC measurements, the samples were heated at 10 °C min⁻¹ from –50 to 200 °C with a modulation period of 60 s and temperature

amplitudes of 1.59 °C. Multiple cycles (*n* ≥ 3) were performed on each sample to ensure the data reproducibility.

Scanning electron microscopy. The morphologies of the materials were characterized by SEM (Ultra 55 field-emission scanning electron microscope, ZEISS). The SEM images were collected with a voltage of 5 kV, and the samples were sputter coated with a thin layer of gold. Multiple images (*n* > 3) were taken at different spots for each sample.

Fourier-transform infrared spectroscopy. FTIR was carried out on a JASCO FTIR 6200 spectrometer (JASCO) equipped with a MIRacle attenuated total reflectance Ge crystal cell in absorbance mode. For each measurement, the spectrum was recorded with 32 scans and a resolution of 4.0 cm⁻¹. Multiple spectra (*n* ≥ 3) were collected for each sample, and for each experimental condition, multiple samples (*n* ≥ 3) were made and characterized. The protein secondary structure contents were determined by performing peak deconvolution over the amide I region (1,600–1,700 cm⁻¹) using Matlab software. The deconvolution was carried out using a secondary derivative method with four primary peaks assigned to a variety of secondary structures respectively: 1,620 cm⁻¹ (β-sheet), 1,645–1,655 cm⁻¹ (random coil/helix), 1,685 cm⁻¹ (β-turn) and 1,698 cm⁻¹ (β-sheet). A Gaussian model was selected for the band shape.

Wide-angle X-ray scattering. Synchrotron WAXS was performed on the BioCars 14BM-C beamline at the Advanced Photon Source at Argonne National Laboratory under proposal GUP-61977. The wavelength of the X-ray beam was 0.979 Å, with a fixed energy of 12.668 keV, and the beam size on the sample was 150 × 300 μm (horizontal × vertical). Data were recorded using an ADSC Quantum 315r detector. The samples-to-detector distance was 200 mm, and the beam stop was 50 mm. An exposure time of 60 s was used for degummed silk fibre and ASN. For silk-based bulk materials, an exposure time of 10 s was used. Background measurement was performed with the sample displaced from the beam, and the image was recorded under the same conditions as used with the sample in the beam. Multiple images (≥ 3) were taken to get better statistics and improve on the signal/background ratio. CeO₂ powder was used for instrument calibration. The 2D wide-angle X-ray diffraction patterns were analysed using the software package FIT2D.

Mechanical properties test. The three-point bending tests were carried out on an Instron 3366 machine in flexural test mode at 25 °C and 50% relative humidity (RH) with a loading rate of 0.2 mm min⁻¹ or 2 mm min⁻¹ for dry specimens and wet specimens, respectively. The specimens had a length of 12 mm, a width of 7 mm and a thickness of 1 mm. Multiple samples (> 3) were tested for each condition.

The tensile tests were carried out on an Instron 3366 machine in tensile test mode at 25 °C and 50% RH with a loading rate of 2 mm min⁻¹. The tested bulk silk samples were in a plate format with a length of 10 mm and a width of 4.3 mm. Multiple samples (> 3) were tested for each condition.

The compression tests were carried out on an Instron 3366 machine in compression test mode at 25 °C and 50% RH with a loading rate of 1 mm min⁻¹. The tested bulk silk samples were in a rod format with a diameter of 3.0 mm and a height of 4.0 mm. Multiple samples (> 3) were tested for each condition.

Fabrication of silk bone screws. Silk bone screws were machined from silk bars using a CNC lathe (Trak TRL 1440 EX, Southwestern Industries). A custom single-point external cutter (Vargud) was used on the CNC lathe to cut screw threads by matching the turning speed with the horizontal speed of the cutter to cut a desired pitch length (outer diameter ~1.8 mm, pitch 600 μm). The screw heads were machined to have a cylindrical head, and a slot was generated.

Fabrication of silk ear tubes. Silk ear tubes were machined from pure silk bars or silk–protease XIV bars (doping ratio ~1 wt%). Each ear tube had a height of ~2.7 mm and a diameter of ~3.2 mm for the head part. The outer and inner diameters for the tubing part were 2.0 mm and 1.0 mm, respectively.

In vitro water uptake and swelling test. Machined silk bone screws (*n* = 3 per condition) were placed in 37 °C PBS for various amounts of time (0 min, 15 min, 60 min, 3 h, 24 h, 48 h, 72 h, 9 d, 15 d and 30 d) and observed for changes in weight and diameter to signify fluid uptake and swelling. Surface moisture was removed from the sample by wiping with a Kimwipe (Kimberly-Clark), the wet weight of the sample was taken (*W*_w) and the head and thread diameters were measured. The water uptake (%) was calculated:

$$\text{Water uptake (\%)} = [(W_s - W_d)/W_s] \times 100 \quad (1)$$

In vitro degradation test. For the in vitro degradation of silk bone screws, machined silk bone screws (*n* = 3 per processing condition) were incubated at 37 °C in PBS solution, 5 U ml⁻¹ protease XIV (Sigma-Aldrich) PBS solution and 40 U ml⁻¹ chymotrypsin (Sigma-Aldrich) PBS solution, respectively. For each silk bone screw, 2 mL of incubation solution was used. The incubation solutions were changed every 2–3 days. At designated time points (2 d, 5 d, 10 d, 20 d, 30 d) groups of

samples were rinsed in deionized water and dried before weighing. The remaining mass of each sample was recorded, and SEM images of the samples were collected.

For the *in vitro* degradation test of the silk ear tubes, machined silk ear tubes ($n = 3$ per processing condition) were incubated at 37 °C in 300 μ l PBS solution. At designated time points (5 min, 1 h, 3 h, 6 h, 24 h, 48 h and 72 h), pictures were taken. After 72 h continuous incubation in PBS solution at 37 °C, the samples were rinsed in deionized water and dried before weighing. The remaining mass of each sample was recorded and analysed.

In vivo biocompatibility test. Machined silk bone screws were sterilized by ethylene oxide prior to implantation. The experimental protocol for animal studies was approved by the Institutional Animal Care and Use Committee of Beth Israel Deaconess Medical Center. For the studies, 13-week female Sprague–Dawley rats (Charles River Laboratories International) were anaesthetized with isoflurane at 5% concentration in oxygen for induction and 2.5% for maintenance. Following anaesthesia, the incision area was shaved and disinfected with a povidone–iodine scrub. A lateral approach was performed via skin incision over the distal 1/3 of the femur followed by incision of the superficial fascia. The intermuscular plane between the vastus lateralis and the biceps femoris muscles was separated. After proper exposure, the lateral cortex of the supracondylar region was drilled using a 1.7 mm drill bit, followed by the insertion of the silk screw. Muscles were then approximated using absorbable sutures (Vicryl 5-0) and skin was closed using skin clips. Buprenorphine was administered at a dosage of 1.2 mg kg⁻¹ pre-op and *pro re nata* (as needed with visible signs of distress). The animals were designated for euthanasia at 1 month after surgery in the CO₂ chamber at the animal facility of the institution. Following euthanasia, the operated femur was harvested and used for micro-computed-tomography (CT) and histology analysis.

Micro-CT analysis. For qualitative 3D evaluation, the distal metaphyseal region of femoral bones was examined by a desktop micro-CT system (μ CT 40, Scanco Medical) using 55 kV peak potential (kVp), 72 μ A current, 250 ms integration time and 30 μ m voxel size. The 3D construction was done considering 200 slides (6 mm bone segment) centred on the screw shaft. Images were acquired at 50% depth of the 3D construct in the sagittal plan to visualize the medullary canal and the screw insertion site. Images were then acquired after applying an X-ray filter to the 3D construction.

Histological analysis. The bone specimens were fixed in 10% neutral buffered formalin at room temperature for 48 h. The fixed specimens were then decalcified in EDTA for 3 to 4 weeks until the bone became flexible. Following decalcification, tissue was processed with ethanol and xylene and then embedded in paraffin on

an automatic processor. Paraffin blocks of each specimen were then sectioned along the long axis of the bone and through the screw. Sections of 5 μ m thickness were baked on glass slides at 60 °C and then stained with hematoxylin and eosin or Masson trichrome stain.

Reporting Summary. Further information on research design is available in the Nature Research Reporting Summary linked to this article.

Data availability

The authors declare that all data supporting the findings of this study are available within the paper and its Supplementary Information files and from the corresponding author upon reasonable request.

Acknowledgements

This work was supported by grants from the National Institutes of Health (R01AR068048, R01DE016525), the Air Force Office of Scientific Research (FA9550-17-1-0333) and the Stepping Strong Foundation, Brigham and Women's Hospital (A. Nazarian and G. Dyer). We thank J. Yarger, B. Cherry and N. Sisco at Arizona State University for help with NMR instrumentation and data collection. We thank G. Dyer for clinical relevance discussions. We also thank S. Maccorkle and D. Dupuis at the Tufts University Machine Shop for materials machining.

Author contributions

C.G., C.L. and D.L.K. conceived and designed the project and experiments; C.G., C.L., H.V.V. and Y.Q. performed the materials fabrication and characterizations; P.H., A.L. and A.N. performed animal studies; C.G., C.L., X.M., S.L. and S.J.L. performed the data analysis and results discussion; D.L.K. supervised the entire project; and C.G. and C.L. wrote the manuscript. All authors discussed the results and commented on the manuscript.

Competing interests

The authors declare no competing interests.

Additional information

Supplementary information is available for this paper at <https://doi.org/10.1038/s41563-019-0560-8>.

Correspondence and requests for materials should be addressed to C.L. or D.L.K.

Reprints and permissions information is available at www.nature.com/reprints.

Reporting Summary

Nature Research wishes to improve the reproducibility of the work that we publish. This form provides structure for consistency and transparency in reporting. For further information on Nature Research policies, see [Authors & Referees](#) and the [Editorial Policy Checklist](#).

Statistics

For all statistical analyses, confirm that the following items are present in the figure legend, table legend, main text, or Methods section.

n/a Confirmed

- | | | |
|-------------------------------------|-------------------------------------|--|
| <input type="checkbox"/> | <input checked="" type="checkbox"/> | The exact sample size (n) for each experimental group/condition, given as a discrete number and unit of measurement |
| <input type="checkbox"/> | <input checked="" type="checkbox"/> | A statement on whether measurements were taken from distinct samples or whether the same sample was measured repeatedly |
| <input type="checkbox"/> | <input checked="" type="checkbox"/> | The statistical test(s) used AND whether they are one- or two-sided
<i>Only common tests should be described solely by name; describe more complex techniques in the Methods section.</i> |
| <input checked="" type="checkbox"/> | <input type="checkbox"/> | A description of all covariates tested |
| <input checked="" type="checkbox"/> | <input type="checkbox"/> | A description of any assumptions or corrections, such as tests of normality and adjustment for multiple comparisons |
| <input type="checkbox"/> | <input checked="" type="checkbox"/> | A full description of the statistical parameters including central tendency (e.g. means) or other basic estimates (e.g. regression coefficient) AND variation (e.g. standard deviation) or associated estimates of uncertainty (e.g. confidence intervals) |
| <input checked="" type="checkbox"/> | <input type="checkbox"/> | For null hypothesis testing, the test statistic (e.g. F , t , r) with confidence intervals, effect sizes, degrees of freedom and P value noted
<i>Give P values as exact values whenever suitable.</i> |
| <input checked="" type="checkbox"/> | <input type="checkbox"/> | For Bayesian analysis, information on the choice of priors and Markov chain Monte Carlo settings |
| <input checked="" type="checkbox"/> | <input type="checkbox"/> | For hierarchical and complex designs, identification of the appropriate level for tests and full reporting of outcomes |
| <input checked="" type="checkbox"/> | <input type="checkbox"/> | Estimates of effect sizes (e.g. Cohen's d , Pearson's r), indicating how they were calculated |

Our web collection on [statistics for biologists](#) contains articles on many of the points above.

Software and code

Policy information about [availability of computer code](#)

Data collection

SEM images were acquired by SmartSEM software (v 05.06). NMR spectra were acquired using VNMRJ software (v 4.0) and Topspin software (v 3.6.1). FTIR spectra were acquired using Spectra Manager software (v 2.0202, JASCO Inc.). Thermal analysis data were collected using TA Advantage software (v 5.5.24). Mechanical properties test data were acquired by Bluehill software (v 3.0, Instron Inc.).

Data analysis

NMR data were analyzed using VNMRJ software (v 4.0) and Topspin software (v 3.6.1). SEM images were analyzed using ImageJ software (v 10.2). Thermal analysis data, mechanical properties test data, X-ray scattering data, and FTIR data were analyzed using MagicPlotPro (v 2.8), FIT2D (v 18.002), and Matlab (v R2017b) softwares. Statistical analysis was done in GraphPad Prism (v 6.0).

For manuscripts utilizing custom algorithms or software that are central to the research but not yet described in published literature, software must be made available to editors/reviewers. We strongly encourage code deposition in a community repository (e.g. GitHub). See the Nature Research [guidelines for submitting code & software](#) for further information.

Data

Policy information about [availability of data](#)

All manuscripts must include a [data availability statement](#). This statement should provide the following information, where applicable:

- Accession codes, unique identifiers, or web links for publicly available datasets
- A list of figures that have associated raw data
- A description of any restrictions on data availability

The authors declare that all data supporting the findings of this study are available within the paper and its Supplementary Information files. Additional data are available from the corresponding author upon reasonable request.

Field-specific reporting

Please select the one below that is the best fit for your research. If you are not sure, read the appropriate sections before making your selection.

Life sciences Behavioural & social sciences Ecological, evolutionary & environmental sciences

For a reference copy of the document with all sections, see [nature.com/documents/nr-reporting-summary-flat.pdf](https://www.nature.com/documents/nr-reporting-summary-flat.pdf)

Life sciences study design

All studies must disclose on these points even when the disclosure is negative.

Sample size	Sample size was determined based on our preliminary data from pilot experiments and previously published results in the literature.
Data exclusions	No data were excluded.
Replication	At least three rats were used for the in vivo study.
Randomization	Rats were assigned randomly to experimental groups.
Blinding	The investigators were not blinded to allocation during experiments and outcome assessment since our data analyses are based on objectively measurable data.

Reporting for specific materials, systems and methods

We require information from authors about some types of materials, experimental systems and methods used in many studies. Here, indicate whether each material, system or method listed is relevant to your study. If you are not sure if a list item applies to your research, read the appropriate section before selecting a response.

Materials & experimental systems

n/a	Involvement in the study
<input checked="" type="checkbox"/>	<input type="checkbox"/> Antibodies
<input checked="" type="checkbox"/>	<input type="checkbox"/> Eukaryotic cell lines
<input checked="" type="checkbox"/>	<input type="checkbox"/> Palaeontology
<input type="checkbox"/>	<input checked="" type="checkbox"/> Animals and other organisms
<input checked="" type="checkbox"/>	<input type="checkbox"/> Human research participants
<input checked="" type="checkbox"/>	<input type="checkbox"/> Clinical data

Methods

n/a	Involvement in the study
<input checked="" type="checkbox"/>	<input type="checkbox"/> ChIP-seq
<input checked="" type="checkbox"/>	<input type="checkbox"/> Flow cytometry
<input checked="" type="checkbox"/>	<input type="checkbox"/> MRI-based neuroimaging

Animals and other organisms

Policy information about [studies involving animals](#); [ARRIVE guidelines](#) recommended for reporting animal research

Laboratory animals	13-week female Sprague–Dawley rats were used. (Charles River Laboratories International, Inc., USA)
Wild animals	No wild animals were used.
Field-collected samples	No field-collected samples were used.
Ethics oversight	All work performed on animals was in accordance with and approved by the Institutional Animal Care and Use Committee (IACUC) of Beth Israel Deaconess Medical Center.

Note that full information on the approval of the study protocol must also be provided in the manuscript.

Reproduced with permission of copyright owner. Further reproduction prohibited without permission.